

# Shape coexistence in the neutron-deficient $^{188}\text{Hg}$ investigated via lifetime measurements

M. Siciliano,<sup>1,2,3</sup> I. Zanon,<sup>1,2,4</sup> A. Goasduff,<sup>2,5</sup> P.R. John,<sup>2,5,6</sup> T.R. Rodríguez-Frutos,<sup>7</sup> S. Péru-Desenfans,<sup>8</sup>  
I. Deloncle,<sup>8,9</sup> J. Libert,<sup>8</sup> M. Zielińska,<sup>3</sup> D. Bazzacco,<sup>5</sup> D. Ashad,<sup>10</sup> G. Benzoni,<sup>11</sup> B. Birkenbach,<sup>12</sup>  
T. Braunroth,<sup>12</sup> A. Boso,<sup>2,5</sup> M. Cicerchia,<sup>1,2</sup> N. Cieplicka-Oryńczak,<sup>11,13</sup> G. Colucci,<sup>2,5</sup> F. Davide,<sup>10</sup>  
G. de Angelis,<sup>1</sup> B. de Canditiis,<sup>10</sup> A. Gadea,<sup>14</sup> L.P. Gaffney,<sup>15</sup> F. Galtarossa,<sup>1,4</sup> A. Gozzelino,<sup>1</sup>  
K. Hadyńska-Klek,<sup>1,16</sup> G. Jaworski,<sup>1,16</sup> P. Koseoglou,<sup>6</sup> S.M. Lenzi,<sup>2,5</sup> B. Melon,<sup>17</sup> R. Menegazzo,<sup>5</sup>  
D. Mengoni,<sup>2,5</sup> A. Nannini,<sup>17</sup> D.R. Napoli,<sup>1</sup> J. Pakarinen,<sup>18</sup> D. Quero,<sup>10</sup> P. Rath,<sup>10</sup> F. Recchia,<sup>2,5</sup>  
M. Rocchini,<sup>17</sup> D. Testov,<sup>2,5,19</sup> J.J. Valiente-Dobón,<sup>1</sup> A. Vogt,<sup>12</sup> J. Wiederhold,<sup>6</sup> and W. Witt<sup>6</sup>

<sup>1</sup>INFN, Laboratori Nazionali di Legnaro, Legnaro, Italy.

<sup>2</sup>Dipartimento di Fisica e Astronomia, Università di Padova, Padova, Italy.

<sup>3</sup>Irfu/CEA, Université de Paris-Saclay, Gif-sur-Yvette, France.

<sup>4</sup>Dipartimento di Fisica e Scienze della Terra, Università di Ferrara, Ferrara, Italy.

<sup>5</sup>INFN, Sezione di Padova, Padova, Italy.

<sup>6</sup>Institut für Kernphysik der Technischen Universität Darmstadt, Darmstadt, Germany.

<sup>7</sup>Universidad Autónoma de Madrid, Madrid, Spain.

<sup>8</sup>CEA, DAM, DIF, Arpajon, France.

<sup>9</sup>IJC lab CNRS/IN2P3, Université de Paris-Saclay, Orsay, France.

<sup>10</sup>Dipartimento di Fisica and INFN Sezione di Napoli, Napoli, Italy.

<sup>11</sup>INFN, Sezione di Milano, Milano, Italy.

<sup>12</sup>Institut für Kernphysik, Universität zu Köln, Cologne, Germany.

<sup>13</sup>Instytut Fizyki Jądrowej im. Henryka Niewodniczańskiego, Polska Akademia Nauk, Krakow, Poland.

<sup>14</sup>Instituto de Física Corpuscular, CSIC-Universidad de Valencia, Valencia, Spain.

<sup>15</sup>University of the West of Scotland, Paisley, Scotland.

<sup>16</sup>Środowiskowe Laboratorium Ciężkich Jonów, Uniwersytet Warszawski, Warsaw, Poland.

<sup>17</sup>Dipartimento di Fisica and INFN Sezione di Firenze, Firenze, Italy.

<sup>18</sup>Fysiikan laitos, Jyväskylän Yliopisto, Jyväskylä, Finland.

<sup>19</sup>Joint Institute for Nuclear Research, Dubna, Russia.

**Background:** Shape coexistence in the  $Z \approx 82$  region has been established in mercury, lead and polonium isotopes. Even-even mercury isotopes with  $100 \leq N \leq 106$  present multiple fingerprints of this phenomenon, which seems to be no longer present for  $N \geq 110$ . According to a number of theoretical calculations, shape coexistence is predicted in the  $^{188}\text{Hg}$  isotope.

**Purpose:** The aim of this work is to measure the lifetime of both yrast and non-yrast excited states of  $^{188}\text{Hg}$  to infer the properties of the belonging bands, such as the deformation. Extending the investigation to the high-lying states, which are expected to be less affected by band-mixing effects, can provide additional information on the coexisting structures.

**Methods:** The  $^{188}\text{Hg}$  nucleus was populated using two different fusion-evaporation reactions with two targets,  $^{158}\text{Gd}$  and  $^{160}\text{Gd}$ , and a beam of  $^{34}\text{S}$ , provided by the Tandem-ALPI accelerators complex at the Laboratori Nazionali di Legnaro. The channels of interest were selected using the information from the Neutron Wall array, while the  $\gamma$  rays were detected using the GALILEO  $\gamma$ -ray array. The lifetimes of the excited states were determined using the Recoil Distance Doppler-Shift method, employing the dedicated GALILEO plunger device.

**Results:** The lifetimes of the states up to spin  $16\hbar$  were measured and the corresponding reduced transition probabilities were calculated. Using the two-bands mixing and rotational models, the deformation of the pure configurations was obtained from the experimental results. The extracted transition strengths were compared with those calculated with the state-of-the-art symmetry-conserving configuration-mixing approach in order to shed light on the nature of the observed structures in the  $^{188}\text{Hg}$  nucleus. An oblate, a normal- and a super-deformed prolate bands were predicted and their underlying shell structure was also discussed.

**Conclusions:** The first lifetime measurements of the high-lying states suggested the presence of an almost spherical structure above the  $12_1^+$  isomer; moreover, they allowed to estimate the structure of the intruder band. The comparison between the extracted transition strengths with the two-band mixing model allowed to infer the deformation of the ground-state band, but the experimental uncertainties do not permit to make firm conclusions on the mixing. The deformation of the oblate and normal-deformed prolate bands, given by the newly-performed theoretical calculations, are in agreement with the experimentally estimated ones. Finally, the comparison with such beyond mean-field calculations also suggested the presence of shape coexistence, not only in  $^{188}\text{Hg}$ , but also in  $^{190}\text{Hg}$ .

PACS numbers: 07.85.Nc, 21.10.Tg, 21.60.-n, 25.60.Pj, 27.70.+q

## I. INTRODUCTION

The regions close to  $Z = 50$  and  $Z = 82$  provide unique conditions to study the evolution of the nuclear shapes and of the collectivity in the vicinity of magic numbers. The lead region, in particular, presents a wide range of phenomena related to the nuclear shape, as for instance shape staggering between odd- and even-mass nuclei [1, 2], shape evolution with mass [3–5] and shape coexistence [6, 7]. The latter is a characteristic feature of finite many-body quantum systems, such as the atomic nucleus, where structures corresponding to different shapes coexist within the typical energy range of nuclear excitations.

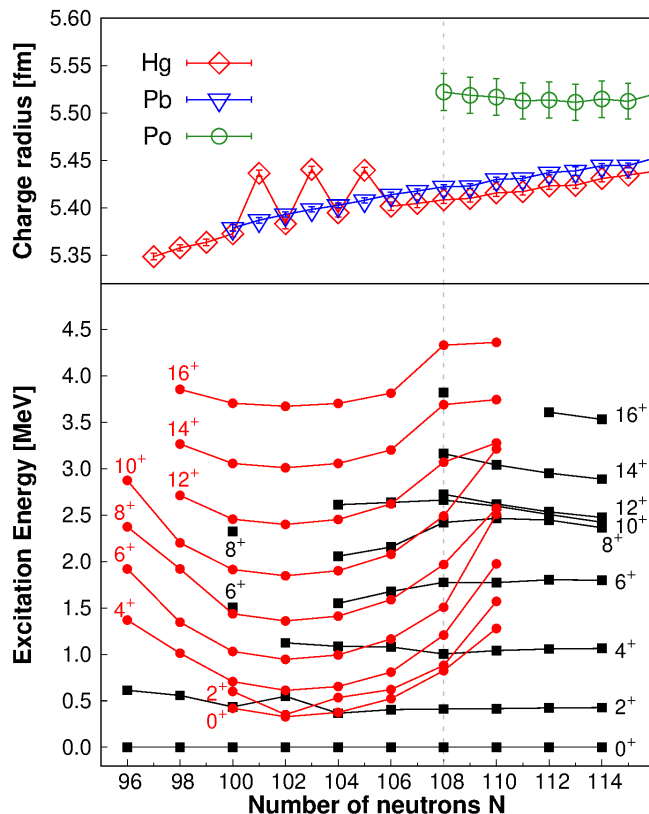


FIG. 1: (Color online) (top) Mean-square charge radius as a function of the neutron number for Po (green), Pb (blue) and Hg (red) isotopic chains. For the  $Z = 80$  isotopes, the large variation of the radius was attributed to the presence of different shapes. Values taken from Refs. [2, 8, 9]. (bottom) Systematics of excited states in the neutron-deficient even-even mercury isotopes, showing (red circles) the assumed intruder and (black squares) ground-state bands. Data taken from the National Nuclear Data Center database [10].

The first hint of shape coexistence in the  $Z \approx 82$  region came from studies of optical hyperfine structure in the neutron-deficient mercury isotopes [8]. As shown in Figure 1 (top panel), significant staggering of the mean-square charge radius were observed for mass  $181 \leq A \leq 185$ , which was interpreted as resulting of the presence of

different deformed structures. This feature of the mean-square charge radius is unique in the nuclear chart and it was confirmed via recent laser-spectroscopy measurements [2], which demonstrated that the shape staggering is present down to  $A = 179$  ( $N = 99$ ), where the nucleus returns to sphericity in its ground state.

Another fingerprint of shape coexistence in mercury isotopes is the observation of low-lying intruder bands built on a second  $0^+$  state, which are particularly close in energy to the ground state in the isotopes from  $^{180}\text{Hg}$  to  $^{188}\text{Hg}$  (see Figure 1 (bottom panel)). From energy levels, the deformation of these nuclei in the ground-state band was estimated to be  $\beta \approx 0.1$ , in contrast to  $\beta \approx 0.3$  obtained for the bands built on the  $0_2^+$  states [11, 12]. These structures tend to mix due to their proximity in energy. The degree of their mixing was first estimated from the measured  $\alpha$ -decay hindrance factors, yielding a 3% admixture of the deformed configuration in the ground state of  $^{180}\text{Hg}$ , while mixing of 16% and 18% was obtained for  $^{182}\text{Hg}$  and  $^{184}\text{Hg}$ , respectively [13]. These mixing strengths are consistent with those deduced from the  $\rho^2(E0; 0_2^+ \rightarrow 0_1^+)$  value for  $^{188}\text{Hg}$  and its upper limit for  $^{186}\text{Hg}$  [14], displaying a parabolic behavior as a function of neutron number with maximum mixing observed at  $N = 104$  mid-shell, where the intruding structure comes the closest in energy to the ground state. The mixing of normal and intruder structures in Hg isotopes was also investigated by applying a phenomenological two-bands mixing model to level energies in observed rotational bands [15, 16]. The most recent study of Ref. [16] accounted for the energies of newly identified non-yrast states in  $^{180,182}\text{Hg}$  and yielded a lower mixing between the  $0^+$  states than that deduced from the  $\alpha$ -decay work of Ref. [13], but still with a maximum around  $N = 102 - 104$ . The conclusions of this analysis for the  $2^+$  states are, however, much different, suggesting an inversion of configurations of the  $2_1^+$  state between  $^{182}\text{Hg}$  and  $^{184}\text{Hg}$ , with almost maximum mixing (51%) for the  $2_1^+$  state in the mid-shell  $^{184}\text{Hg}$  nucleus. Again, when moving away from  $N = 104$ , both towards lighter and heavier nuclei, the configurations of the  $2^+$  states become more pure. The importance of configuration mixing in the structure of  $2^+$  states in neutron-deficient Hg nuclei is again supported by enhanced  $\rho^2(E0; 2_2^+ \rightarrow 2_1^+)$  transition strengths observed for  $^{180}\text{Hg}$  [17],  $^{182}\text{Hg}$  [18],  $^{184}\text{Hg}$  [18] and  $^{186}\text{Hg}$  [19, 20]. Finally, the mixing of states with  $J > 2$  extracted from the perturbation of level energies in rotational bands in  $^{180,188}\text{Hg}$  [16] decreases interestingly with spin and it no longer displays a parabolic behavior as a function of neutron number, but rather a monotonic increase with mass (e.g. for the  $4^+$  states the mixing goes from 2% in  $^{180}\text{Hg}$  to 20% in  $^{188}\text{Hg}$ ). Currently no E0 transition strengths are known in neutron-deficient Hg nuclei between the states of spin 4 and higher.

Further information on collective structures in neutron-deficient Hg nuclei was provided by measurements of  $\gamma$ -ray transition strengths. Lifetimes of the ex-

cited states were measured for several neutron-deficient species, populated via fusion-evaporation reactions: the  $^{178}\text{Hg}$  [21],  $^{180,182}\text{Hg}$  [22, 23] and  $^{184,186}\text{Hg}$  [16, 24, 25] nuclei were studied using the Recoil-Distance Doppler-Shift (RDDS) method, while the Doppler-Shift Attenuation Method (DSAM) and the  $\beta$ -tagged fast-timing (FT) techniques were employed to investigate  $^{184}\text{Hg}$  [26] and  $^{186,188}\text{Hg}$  [14, 27] isotopes, respectively. Moreover, the lifetimes of the low-lying states in  $^{190-196}\text{Hg}$  isotopes, which could not be investigated via RDDS method due to the presence of low-lying isomers, was recently measured via the FT technique [27, 28]. These studies were mostly limited to yrast states but, as the intruder band becomes yrast at low spin (see Figure 1 (bottom panel)), they yielded lifetimes of states in both coexisting bands in the even-mass  $^{180-186}\text{Hg}$  nuclei, providing strong support for the very different deformations of these two structures.

Finally, with the advent of radioactive ion-beam facilities, the even-mass  $^{182-188}\text{Hg}$  isotopes were investigated via low-energy Coulomb excitation, yielding magnitudes and signs of the reduced E2 matrix elements between the low-lying excited states [29, 30]. Combined with the mixing coefficients of Ref. [16], these results provided a consistent picture of two distinct configurations (weakly-deformed oblate and strongly-deformed prolate) contributing in varying proportions to the observed low-lying states in  $^{182-188}\text{Hg}$ . Even though the simplest observables, such as the energy of the first-excited  $2^+$  state and the  $B(E2; 2_1^+ \rightarrow 0_1^+)$  value, are almost identical in  $^{182-188}\text{Hg}$ , the structures of  $2_1^+$  states were demonstrated to be very different: the intruder configuration dominates in  $^{182}\text{Hg}$ , both configurations almost equally contribute in  $^{184}\text{Hg}$  and the normal configuration prevails for  $^{186,188}\text{Hg}$ . Unfortunately, due to strong correlations between the reduced matrix elements, the important role of E0 transitions between the  $2^+$  states and the lack of sufficiently precise lifetimes, branching and mixing ratios for the nuclei of interest, it was not possible to determine any spectroscopic quadrupole moments from this study, except for the  $Q_s(2_1^+) = 0.8^{+0.5}_{-0.3}$  eb in  $^{188}\text{Hg}$ , suggesting an oblate deformation of this state.

The first interpretation of the intruder band was given in the work of C. Prahara and S. Khadkikar [31], who performed Hartree-Fock calculations for even-mass mercury isotopes from  $A = 184$  to  $A = 204$  and obtained  $\beta$  deformation parameters for the two coexisting structures. In their calculations, all these nuclei present oblate ground-state bands, with a maximum of the deformation for  $A = 186$  ( $\beta = 0.117$ ), while the excited bands are prolate-deformed. In particular, small mixing was predicted between the two bands in  $^{188}\text{Hg}$ . More recently, Nikšić and collaborators performed relativistic Hartree-Bogoliubov (RHB) calculations [32] and predicted the ground-state band of Hg isotopes to be weakly-deformed oblate, due to the two-protons hole in the  $Z = 82$ . Then, for the isotopes close to the neutron mid-shell, including  $^{188}\text{Hg}$ , this oblate ground-state band was predicted to be crossed by the intruding prolate-deformed band,

related to  $4p - 6h$  proton excitations into the  $h_{9/2}$  and  $f_{7/2}$  orbitals, and the two structures were expected to be strongly mixed. Similar conclusions could also be reached from beyond mean-field (BMF) calculations and interacting boson models (IBM), that have been summarized in the works of N. Bree et al. [29] and K. Wrzosek-Lipska et al. [30]. In their works, the BMF approach predicts for  $N \geq 106$  a weakly-deformed ground-state band coexisting with an excited prolate band characterized by a stronger deformation. For nuclei with  $100 \leq N \leq 104$  the two bands cross and the ground state is expected to be predominantly prolate, while the first excited  $0^+$  state is predicted to have equal contributions of the oblate and the prolate configuration.

The intruder structure of  $^{188}\text{Hg}$  appears at excitation energy slightly higher than in  $^{182-186}\text{Hg}$ , but it also becomes yrast very quickly, starting from spin  $6^+$ . The degree of mixing between the two coexisting structures is expected to be lower than at mid-shell, but the detailed predictions of the models significantly differ. As  $^{188}\text{Hg}$  is less exotic and thus easier accessible for high-precision spectroscopy than the Hg isotopes in the nearest vicinity of  $N = 104$ , the paucity of information about its electromagnetic structure, in particular that of higher-spin states, is surprising. The transition probabilities in  $^{188}\text{Hg}$  were studied via lifetime measurements using the FT technique [14, 27] and via Coulomb excitation [29, 30], but the existing information is mostly limited to yrast states and the results on the  $2_1^+$  lifetime are not consistent. In order to obtain a clear picture of shape coexistence in  $^{188}\text{Hg}$  and a deeper insight into configuration mixing in Hg nuclei, precise determination of the reduced transition probabilities between the low-lying states, belonging to both structures, is mandatory.

In the present paper, the lifetime measurement of the excited states in both the ground-state and intruder bands are presented for  $^{188}\text{Hg}$ . The results are discussed and interpreted in the context of new beyond mean-field calculations performed via the symmetry-conserving configuration-mixing method.

## II. EXPERIMENTAL DETAILS

Two experiments were performed, using different fusion-evaporation reactions, to populate the excited states in  $^{188}\text{Hg}$ . In the first one, a  $^{34}\text{S}$  beam at 185-MeV energy impinged on a  $600 \mu\text{g}/\text{cm}^2$  thick target of  $^{160}\text{Gd}$ , evaporated onto a  $2.5 \text{ mg}/\text{cm}^2$  thick  $^{181}\text{Ta}$  fronting. The second one used a  $^{34}\text{S}$  beam at the energy of 165 MeV and a  $600 \mu\text{g}/\text{cm}^2$  thick target of  $^{158}\text{Gd}$  with an identical fronting. In the following, these two measurements will be referred to as *Exp.1* and *Exp.2*, respectively. As the cross sections for individual reaction channels were different for *Exp.1* and *Exp.2*, this approach provided a better control of possible contamination in the  $^{188}\text{Hg}$  data by other reaction channels. The  $^{34}\text{S}$  beam was provided by the Tandem-ALPI accelerator complex [33, 34] of the

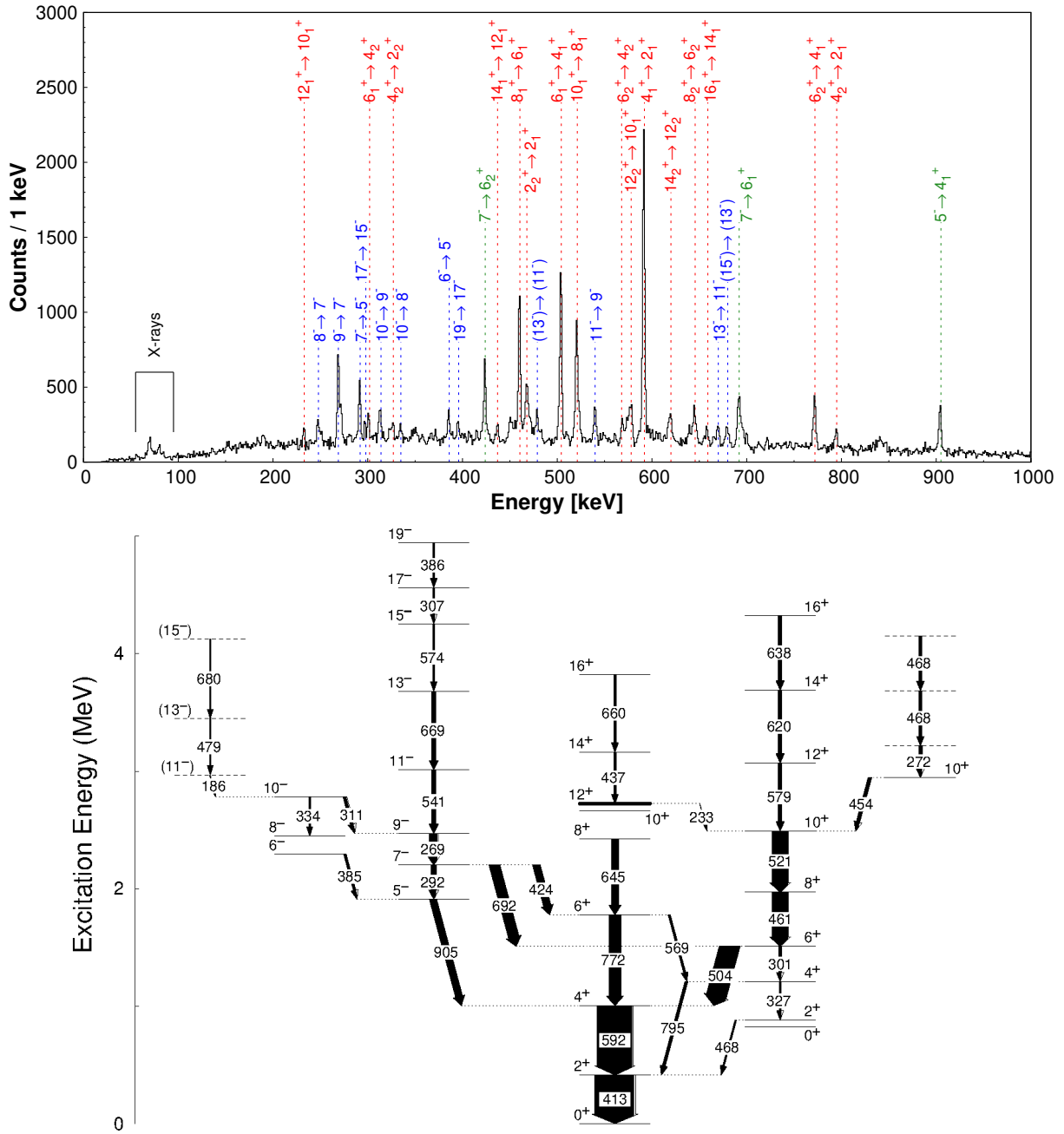


FIG. 2: (Color online) (top) Background-subtracted  $\gamma$ -ray energy spectrum from the GALILEO detectors at  $90^\circ$ , obtained by gating on the 413-keV  $2_1^+ \rightarrow 0_{g.s.}^+$  transition and requiring the coincidence with at least one neutron. The statistics is the sum of the *Exp.1* and *Exp.2* datasets. The identified transitions in the  $^{188}\text{Hg}$  positive-parity bands are marked in red, those in and between negative-parity bands are highlighted in blue, while those between positive-parity and negative-parity bands are in green. (bottom) Partial level scheme of  $^{188}\text{Hg}$ , reporting the identified  $\gamma$ -ray transitions. The arrows widths represent the efficiency-corrected transition yields.

Laboratori Nazionali di Legnaro (Italy). The  $\gamma$  rays were detected by the GALILEO spectrometer, an array of 25 Compton-shielded HPGe detectors, arranged into 3 rings at backward angles ( $152^\circ$ ,  $129^\circ$ ,  $119^\circ$ ) and one ring at  $90^\circ$  [35]. The neutrons evaporated in the reaction were detected using the Neutron Wall array [36], composed of 45 liquid scintillators placed at forward angles with re-

spect to the beam direction. The use of Neutron Wall was necessary to discriminate between the events of interest, expected in coincidence with at least one neutron, and the Coulomb-excitation background [37]. Figure 2 (top panel) shows the  $\gamma$ -ray energy spectrum of  $^{188}\text{Hg}$ , obtained in coincidence with at least one neutron and gated on the  $2_1^+ \rightarrow 0_{g.s.}^+$  transition in  $^{188}\text{Hg}$ . The partial

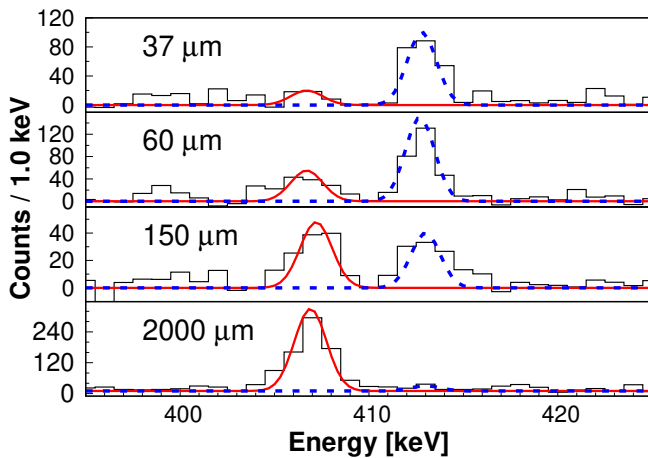


FIG. 3: (Color online) Background-subtracted  $\gamma$ -ray energy spectra of  $^{188}\text{Hg}$  as a function of different target-to-stopper distances for the *Exp.2* dataset and the GALILEO detectors at  $152^\circ$ . The spectra are obtained by gating on the in-flight component of the  $4_1^+ \rightarrow 2_1^+$  transition and requiring the coincidence with at least one neutron. The in-flight and stopped components are indicated by solid-red and dashed-blue lines, respectively.

level scheme, showing all the  $\gamma$ -ray transitions observed in the present study, is presented in the bottom panel of Figure 2. More details about the pre-sorting of the data can be found in Ref. [38].

For the lifetime measurements, the RDDS technique [39] was used by employing the GALILEO plunger [40] with a 11 mg/cm<sup>2</sup> thick  $^{197}\text{Au}$  stopper mounted after the target. For each  $\gamma$ -ray transition two components were observed, related to the radiation emitted before and at the  $^{197}\text{Au}$  foil: the  $\gamma$  rays emitted in-flight after the target are Doppler shifted, while those emitted after the implantation in the stopper are detected at the proper energy. From the energy difference between the in-flight and the stopped components of the  $\gamma$ -ray transitions, the average velocity of the  $^{188}\text{Hg}$  evaporation residue (ER) was determined, being  $\beta = 1.71(8)\%$  for *Exp.1* and  $\beta = 1.59(1)\%$  in *Exp.2*. Considering the velocity of the nucleus of interest, seven target-stopper distances in the range 20-600  $\mu\text{m}$  were used during the *Exp.1* and seven in the range 7-2000  $\mu\text{m}$  during *Exp.2*, to measure lifetimes between few and tens of picoseconds. Specifically, for the first experiment the distances were optimized to get information mostly on the  $2_1^+$  excited state, while for the second they were selected to extend the measurement also to shorter-lived states.

### III. LIFETIME ANALYSIS

In order to avoid the effects of unobserved feeding transitions and to reduce the possibility of contamination from different reaction channels, the lifetime measurements were performed using the  $\gamma$ - $\gamma$  coincidence procedure, gating on the in-flight component of the most

intense feeding transition. Moreover, in order to filter out the events resulting from the Coulomb excitation of both  $^{197}\text{Au}$  stopper and  $^{181}\text{Ta}$  target fronting, all the analyzed  $\gamma$ - $\gamma$  matrices were constructed by requiring the coincidence with at least one neutron identified in the Neutron Wall array. Figure 3 shows the evolution of the intensities of the in-flight and stopped peaks of the  $2_1^+ \rightarrow 0_{g.s.}^+$  transition as a function of the target-degrader distance, after gating on the  $4_1^+ \rightarrow 2_1^+$  in-flight component. The lifetimes of the states were extracted using the NAPATAU software [41], applying the Differential Decay Curve Method (DDCM) [39] by fitting the area of both the in-flight ( $I_i^{if}$ ) and the stopped ( $I_i^{st}$ ) components with a polynomial piecewise function. These intensities were scaled according to an external normalization, given by the area of the 136-keV  $\gamma$ -ray peak of  $^{181}\text{Ta}$ . This choice for the normalization was due to the fact that the number of counts in this peak is not only proportional to the beam intensity and duration of the run, but it also provides a measure of possible degradation of the target during the experiment.

The lifetime  $\tau_i$  should be constant for each  $i$ -th target-stopper distance and it is obtained as

$$\tau_i = \frac{I_i^{st} - \sum_j (Br \alpha I_i^{st})_j}{\frac{d}{dt} I_i^{if}}, \quad (1)$$

where the summation is extended over the  $j$  feeding transitions, each with a certain branching ratio ( $Br$ ) and parameter  $\alpha$ , which includes the efficiency correction and the angular correlation between the transition of interest and the feeding one. In the case of the  $\gamma$ - $\gamma$  coincidence procedure with gating on the in-flight component of the feeding transition, the contributions from feeding transitions are eliminated and this term is null. The final result is given by the weighted average of the lifetimes within the sensitive region of the technique, i.e. where the derivative of the fitting function is larger.

The lifetimes of the  $J^\pi = 2_1^+, 4_1^+, 6_1^+, 8_1^+, 10_1^+, 14_1^+$  and  $16_1^+$  excited states in  $^{188}\text{Hg}$  were extracted via the DDCM by gating on the in-flight component of the  $(J^\pi + 2) \rightarrow J^\pi$  feeding transition. The lifetime of these states was obtained for each of the three GALILEO rings separately and then the weighted average was calculated, except for the  $16^+$  state where the statistics from the three rings had to be summed. In Figure 4 the DDCM analysis performed for the  $2_1^+$  state is presented for *Exp.1* and *Exp.2*, showing the results for the detectors at  $129^\circ$  and  $152^\circ$ , respectively. The lifetimes obtained from the two datasets and the three HPGe rings are in a perfect agreement. Thus, the weighted average of the results obtained for the different detectors angles were calculated, leading to  $\tau(2_1^+) = 25(2)$  ps for *Exp.1*,  $\tau(2_1^+) = 24(1)$  ps for *Exp.2*. The lifetime of the  $4_1^+$  state could be determined only from the *Exp.2* dataset, which yielded  $\tau(4_1^+) = 1.9(8)$  ps. These results are in agreement with literature [27, 29, 30].

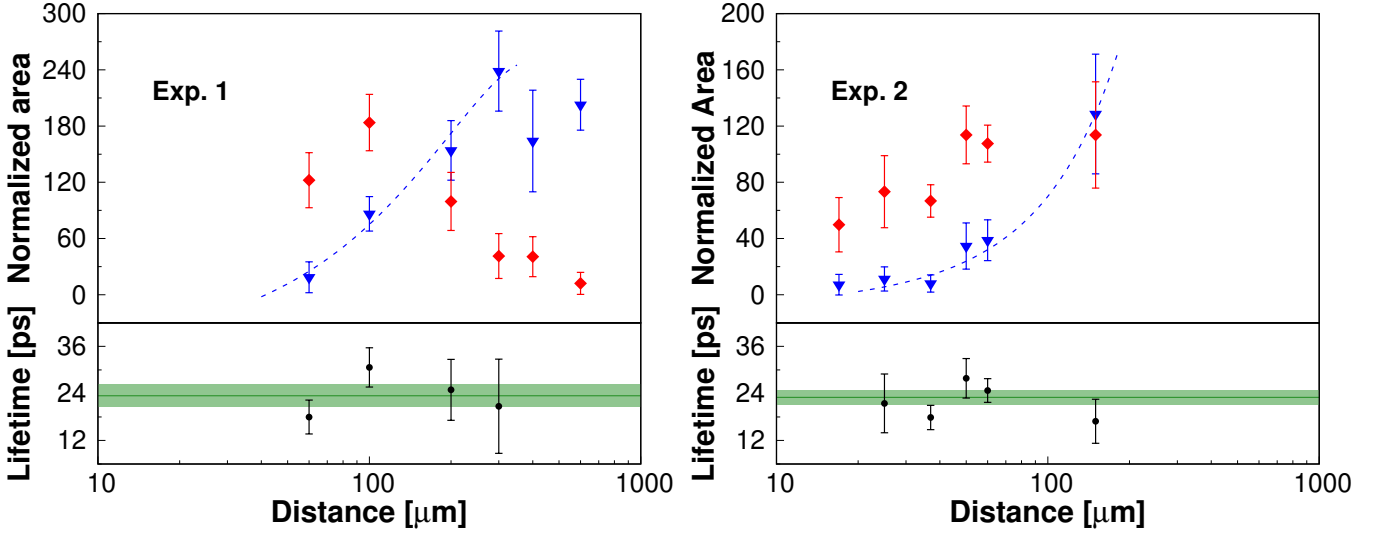


FIG. 4: (Color online) DDCM analysis for the lifetime measurement of the  $2_1^+$  excited state, after gating on the in-flight component of the  $4_1^+ \rightarrow 2_1^+$  transition. (top) Area of the (blue) in-flight and (red) stopped components, normalized over the intensity of the 136-keV peak of  $^{181}\text{Ta}$ . The dashed lines represent the curves fitting the in-flight-component points in the sensitive region of the technique. (bottom) Corresponding lifetimes obtained for individual distances. The solid line denotes the weighted average of the lifetimes, while the filled area corresponds to  $1\sigma$  uncertainty.

Due to the high spin of the state, the limited statistics (see Figure 2) collected for the distances sensitive to lifetime of the  $12_2^+$  excited state hindered its precise measurement. From the only two experimental points,  $\tau(12_2^+) \approx 2$  ps was estimated, which would be consistent with the trend observed for the transitional quadrupole moments in the high-spin part of the intruder band (see Table II); however, due to an insufficient number of experimental points in the sensitive range of the method, it has been decided to adopt a more conservative upper limit of 4 ps for this state.

The presence of the 154-ns  $12_1^+$  isomeric state prevented the investigation of the  $J^\pi = 10_2^+, 8_2^+, 6_2^+$  states with the RDDS technique. From *Exp.1* and *Exp.2* mea-

surements, an upper limit of 10 ps can be set for the  $6_2^+$  excited state, since in the spectra gated on both the 645-keV  $8_2^+ \rightarrow 6_2^+$  and the 424-keV  $7^- \rightarrow 6_2^+$  transitions only the in-flight component of the  $6_2^+ \rightarrow 4_1^+$  transition was clearly observed for the longer plunger distances.

Due to the insufficient level of statistics in the 301-keV  $6_1^+ \rightarrow 4_2^+$  transition, it was not possible to extract the lifetime of the  $4_2^+$  state via the DDCM. Thus, for the *Exp.2* dataset a different gate on the 460-keV  $8_1^+ \rightarrow 6_1^+$  transition was set and the lifetime was extracted via the Decay-Curve Method (DCM), using a second-order Bateman equation and taking into account the contribution of the  $6_1^+$  state. Figure 5 shows the decay curve for the  $4_2^+$  state, resulting in a lifetime of  $\tau(4_2^+) = 8(3)$  ps.

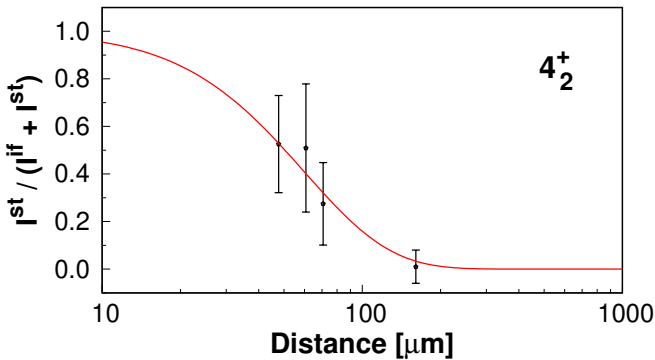


FIG. 5: (Color online) Decay curve of the  $4_2^+$  excited state in  $^{188}\text{Hg}$  as a function of the target-stopper distance, obtained for the *Exp.2* dataset by gating on the in-flight component of the  $8_1^+ \rightarrow 6_1^+$  transition (see text). The red line represents the fitted decay curve, assuming  $\tau(6_1^+) = 5.1(5)$  ps.

TABLE I: Lifetimes (in picoseconds) of the  $J_i^\pi$  excited states in  $^{188}\text{Hg}$ . The weighted averages of the results from the three GALILEO rings are given and compared with literature [27, 29, 30]. The reported uncertainties are statistical only.

$J_i^\pi$	<i>Exp.1</i>	<i>Exp.2</i>	<i>Previous</i>
$2_1^+$	25(2)	24(1)	19(3)
$4_1^+$	-	1.9(8)	2.3(2)
$4_2^+$	< 10	8(3)	< 58
$6_1^+$	5.5(6)	5.1(5)	< 14
$6_2^+$	< 10	< 10	< 30
$8_1^+$	-	2.7(2)	-
$10_1^+$	-	2.1(2)	-
$12_2^+$	-	< 4	-
$14_1^+$	18(4)	19(3)	-
$16_1^+$	< 20	12(3)	-

Table I summarizes the experimental results from the two datasets. The reported uncertainties represent the



$1\sigma$  statistical error, given by the adopted procedures and the weighted average of the results from the individual GALILEO rings. Additionally, a systematic uncertainty (typically  $\leq 3\%$ ), accounting for the choice of the fitting function and relativistic effects [39], should be considered. Because of the longer distances investigated in *Exp.1*, it was possible to study only for the lifetimes of the  $2_1^+$ ,  $6_1^+$  and  $14_1^+$  excited states. Then, similarly to the discussed  $6_2^+$  case, only an upper limit can be set for the  $4_2^+$  and  $16_1^+$  states.

#### IV. DISCUSSION

From the weighted average of lifetimes ( $\bar{\tau}$ ) measured in *Exp.1* and *Exp.2*, corresponding  $B(E2)$  strengths can be extracted. They can be further related to the deformation parameters using simple rotational approximations.

In the axially symmetric rotor model, the transition quadrupole moment  $Q_t$  is related to the E2 transition probability via

$$B(E2; J_i \rightarrow J_f) = \frac{5}{16\pi} \langle J_i, K, 2, 0 | J_f, K \rangle^2 Q_t^2, \quad (2)$$

where  $J_f = J_i - 2$  and  $\langle J_i, K, 2, 0 | J_f, K \rangle$  is the Clebsch-Gordan coefficient.  $K$  is the spin projection along the symmetry axis of the nucleus, conserved in the case of axial symmetry (thus it is equal to 0 for the considered states in both coexisting structures in  $^{188}\text{Hg}$ ). Under this assumption,  $Q_t$  does not change within a band and it is equal to the intrinsic quadrupole moment  $Q_0$ , which is related to the  $\beta_2$  deformation parameter via

$$Q_0 = \frac{3}{\sqrt{5\pi}} Z R_0^2 \beta_2 (1 + 0.16\beta_2), \quad (3)$$

where  $R_0 = 1.20A^{1/3}$ .

In Table II the  $B(E2)$  transition strengths and the corresponding  $Q_t$  and  $\beta_2$  values are reported for the in-band transitions. Based on the excitation energies of the states and the  $Q_t$  values, three different rotational-like configurations can be identified: a slightly-deformed ground-state structure below the  $12_1^+$  isomeric state, an almost-spherical ground-state structure above it and finally the deformed intruder band. For the latter, within the experimental uncertainties, the quadrupole moments tend to be constant for the  $J \geq 4$  states ( $Q_t \approx 5.88$  eb, which corresponds to  $\beta_2 \approx 0.21$ ). The rather constant trend of the quadrupole moments suggests that, even for the lower-spin states, the mixing between the coexisting normal and intruder bands seems limited and not variable with spin, since the latter exhibits characteristics of a perfect axial rotor. Therefore a first estimate of reduced transition probabilities in the pure intruder structure can be obtained using the average  $Q_t$  value for higher-spin states in the intruder band, as shown in Figure 6.

Since there is substantial experimental evidence for the mixing between the ground-state and the intruder bands (e.g. significant  $\rho^2(E0)$  values, intense intra-band transitions), it is reasonable to assume that the two structures are not axially symmetric. Thus, assuming that the  $J \geq 4$  intruder states result from a rotation of a non-axial nucleus characterized by two deformation parameters ( $\beta_2, \gamma$ ), one can relate the measured  $B(E2)$  values to the intrinsic quadrupole moment  $Q_0$  using the following extension of Equation (2):

$$B(E2; J \rightarrow J-2) = \frac{5}{8\pi} Q_0^2 \frac{J(J-1)}{(2J-1)(2J+1)} \times \left[ \cos(\gamma + 30^\circ) - \frac{\langle K^2 \rangle}{(J-1)J} \cos(\gamma - 30^\circ) \right]^2. \quad (4)$$

Applying the described model to the measured  $B(E2)$  values for  $J \geq 4$ , one obtains for the pure intruder configuration  $Q_0 = 5.90(22)$  eb (corresponding to  $\beta_2 = 0.21(1)$ ) and  $\gamma = 14(2)^\circ$ . Here, we again assumed  $K = 0$  for all states in the intruder band, as the departure from axial symmetry is not large and  $K$  is likely to be approximately a good quantum number.

In order to shed light on the structure of the coexisting configurations, accounting for the mixing between them, the experimental reduced transition probabilities are further compared with a band-mixing model [42] and with beyond mean-field calculations.

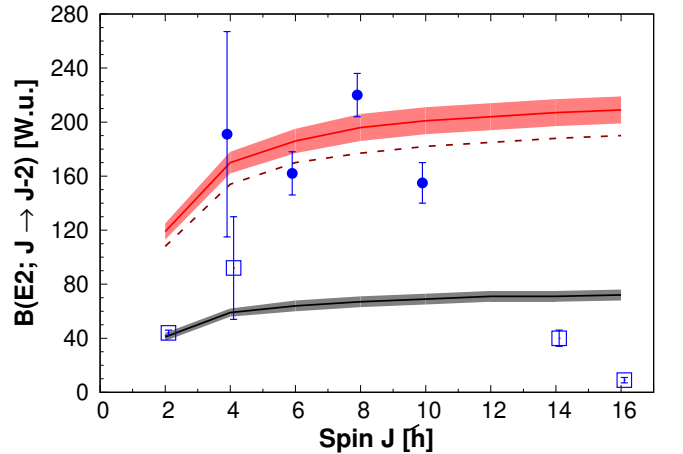


FIG. 6: (Color online) Measured  $B(E2)$  values as a function of spin are compared with those calculated from the two-bands mixing model [42]. The black (red) solid line denotes pure normal (intruder) structures transition strengths, while the related shaded areas correspond to their error bars. The  $B(E2)$  values for the pure intruder configuration, estimated from the axially symmetric rotor model (see text) are presented with a dashed red line. The open squares and the solid circles represent the experimental values for the normal and intruder bands, respectively.

TABLE II: Comparison between the reduced transition probabilities  $B(E2; J_i^\pi \rightarrow J_f^\pi)$ , extracted from the measured lifetimes, and the theoretical values predicted by IBM-CM [43] and SCCM for  $^{188}\text{Hg}$ . The transition quadrupole moment  $Q_t$  and the  $\beta_2$  deformation parameter are extracted assuming an axial symmetric rotor model. The experimental values marked with  $^{(a)}$  and the branching ratios ( $Br$ ) are taken Ref. [44].

$J_i^+ \rightarrow J_f^+$	$E_\gamma$ [keV]	$\bar{\tau}$ [ps]	$Br$	$B(E2)$ [W.u.]			$ Q_t $ [eb]	$\beta_2$
				$Exp.$	$IBM-CM$	$SCCM$		
$2_1^+ \rightarrow 0_1^+$	413	24.4(9)	1.00	44(2)	54	60	3.66(10)	0.128(4)
$4_1^+ \rightarrow 2_1^+$	592	1.9(8)	1.00	92(38)	74	94	4.5(13)	0.158(47)
$6_2^+ \rightarrow 4_1^+$	772	< 10	0.78(1)	> 4	-	-	> 0.85	> 0.03
$12_1^+ \rightarrow 10_2^+$	62	$^{(a)}222(29) 10^3$	1.00	1.3(2)	-	-	0.50(5)	0.017(2)
$14_1^+ \rightarrow 12_1^+$	437	19(3)	1.00	40(6)	-	-	2.73(31)	0.095(11)
$16_1^+ \rightarrow 14_1^+$	659	12(3)	1.00	8(2)	-	-	1.24(22)	0.043(8)
$4_2^+ \rightarrow 2_2^+$	327	8(3)	0.46(2)	191(76)	151	316	6.56(184)	0.23(6)
$6_1^+ \rightarrow 4_2^+$	301	5.3(3)	0.16(1)	156(14)	126	355	5.65(36)	0.20(2)
$8_1^+ \rightarrow 6_1^+$	461	2.7(2)	1.00	220(16)	268	382	6.56(35)	0.23(1)
$10_1^+ \rightarrow 8_1^+$	521	2.1(2)	1.00	155(15)	272	-	5.42(37)	0.19(1)
$12_2^+ \rightarrow 10_1^+$	578	< 4	1.00	> 48	262	-	> 3.00	> 0.10
$2_2^+ \rightarrow 0_1^+$	881	$^{(a)}203(45)$	0.60(3)	0.08(2)	0.8	0.4	-	-
$6_1^+ \rightarrow 4_1^+$	504	5.3(3)	0.79(1)	57(4)	130	1.5	-	-

### A. Two-bands mixing

The assumption of a purely rotational character of the high-spin intruder states is in line with the work of L.P. Gaffney et al. [16] where, considering a spin-independent interaction between two rotational structures and employing the method of Ref. [42], the mixing strengths ( $\alpha_{mix}$ ) for the excited states up to spin  $10\hbar$  were extracted from the excitation energies. The  $6_1^+$ ,  $8_1^+$  and  $10_1^+$  excited states were estimated to have admixture of the normal structure at the level of 6.1%, 1.2% and 0.5%, respectively.

By applying the two-bands mixing model [42] to the transition probabilities determined from the presently measured lifetimes, information on the pure normal and intruder configurations can be obtained. Indeed, such a two-state mixing model is a simple approach to interpret the properties of physical states based on the mixing of different intrinsic configurations. As extensively discussed in the work of E. Clément et al. [45], under the assumption of two rotational structures not linked by any transition between the intrinsic states of the different bands, the experimentally observed states  $|J_{1,2}^\pi\rangle$  can be written as a linear combination of the intrinsic pure prolate ( $|J_{pr}^\pi\rangle$ ) and oblate states ( $|J_{ob}^\pi\rangle$ ):

$$\begin{aligned} |J_1^\pi\rangle &= \alpha_{mix}|J_{ob}^\pi\rangle + \sqrt{1 - \alpha_{mix}^2}|J_{pr}^\pi\rangle \\ |J_2^\pi\rangle &= -\sqrt{1 - \alpha_{mix}^2}|J_{ob}^\pi\rangle + \alpha_{mix}|J_{pr}^\pi\rangle. \end{aligned} \quad (5)$$

Adopting the experimentally-deduced mixing strengths of Ref. [16], the resulting normal structure is characterized by  $|Q_0^n| = 3.66(37)$  eb ( $\beta_2 \approx 0.13$ ) and the intruder one by  $|Q_0^i| = 6.42(45)$  eb ( $\beta_2 \approx 0.22$ ). However, Figure 6 shows that the experimental reduced transition probabilities manifest a smaller mixing than

that estimated in Ref. [16] from the excitation energies of the states.

### B. Beyond mean-field calculations

The reduced transition probabilities have been first compared with the theoretical calculations obtained with an Interacting-Boson Model with Configuration Mixing (IBM-CM) [43]. The model allows the simultaneous treatment and mixing of several boson configurations which correspond to different particle-hole excitations: two-protons excitation across the  $Z = 82$  closed shell is considered. For the  $\gamma$ -ray transitions within the same band a good agreement with the experimental results is observed, while an overestimation of the  $B(E2; 6_1^+ \rightarrow 4_1^+)$  value might suggest an experimental mixing lower than the one predicted by the calculations. However, in line with the results of various mean-field calculations for the Hg nuclei [32, 46, 47], IBM-CM fails to reproduce the shape of the light Hg isotopes: while experimental data provide evidence that for mass  $180 \leq A \leq 188$  the ground-state band is oblate and the intruder band is prolate, the model predicts a prolate energy minimum for the even-even  $^{180-184}\text{Hg}$ , a degenerate prolate-oblate one for  $^{186}\text{Hg}$  and an oblate ground state for  $A \geq 188$ .

In the view of the measured lifetimes, many of them obtained for the first time, the neutron-deficient  $^{186,188,190}\text{Hg}$  have also been studied within a self-consistent beyond mean-field framework, i.e. the so-called symmetry conserving configuration mixing (SCCM) method with the Gogny D1S interaction [48, 49]. These calculations are based on the mixing of a set of intrinsic states with different quadrupole deformations. These intrinsic states are Hartree-Fock-Bogoliubov (HFB) like wave functions obtained self-



consistently through the particle-number variation after projection (PN-VAP) method [50]. Because the HFB states also break the rotational invariance of the system, this symmetry is restored by projecting onto good angular momentum (particle-number and angular momentum projection, PNAMP). The final spectrum and nuclear wave functions are obtained by mixing such PNAMP states within the generator coordinate method (GCM). The region under study is expected to show competing shapes in the low-lying spectrum. This kind of systems could be particularly sensitive to the convergence of the calculations with the number of harmonic oscillator shells,  $N_{h.o.}$ , used to define the HFB transformation [51]. We performed SCCM calculations exploring the axial quadrupole ( $\beta_2$ ) degree of freedom with  $N_{h.o.} = 11, 13, 15$  and  $17$  and only with the latter value the convergence of the energies and wave functions was guaranteed. Such a large number of harmonic oscillator shells makes the SCCM with triaxial shapes extremely expensive from the computational point of view and only axial SCCM results are reported here.

A first glance at the structure of the  $^{186,188,190}\text{Hg}$  isotopes can be obtained by analysing the PN-VAP and PNAMP energies as a function of the deformation  $\beta_2$ . We observe in Figure 7 that the three nuclei show two clear minima, corresponding to oblate ( $\beta_2 \approx -0.17$ ) and prolate superdeformed (SD) ( $\beta_2 \approx +0.65$ ) shapes, and a double minimum structure around normal-deformed (ND) prolate configurations with  $\beta_2 \approx +0.1, +0.3$ . Once the angular momentum projection is performed, in the three cases, the absolute minimum for  $J = 0$  is the oblate one, then the ND states and, finally, the SD configuration. Oblate and ND minima are rather close in energy in  $^{186}\text{Hg}$ , while ND and SD minima are almost degenerated in  $^{190}\text{Hg}$ .

These energy surfaces suggest the presence of shape coexistence and/or shape mixing in these nuclei. However, the final theoretical spectra are obtained by mixing the PNAMP states with different quadrupole deformations. Excitation energies for the three nuclei are plotted in Figure 8 and the collective wave functions (CWF) (i.e., the weights of the intrinsic quadrupole deformations in each nuclear state) are represented in Figure 9. The position of the energies on the  $x$ -axis corresponds to the mean value of the intrinsic quadrupole deformation for each state provided by the CWFs. Here, we clearly observe for the three isotopes the three different collective bands (with  $\Delta J = 2$ ) associated to the oblate (ground state bands), ND-prolate and SD-prolate minima. The excitation energy of the  $0_2^+$  state is lower for the lighter isotope, suggesting a considerable shape-coexistence in  $^{186}\text{Hg}$ . Additionally, a  $0_2^+$  state is also found close to the band-head of the SD band for  $^{190}\text{Hg}$ . Hence, the  $0_2^+$  excitation energy associated to the ND band is expected to be larger in  $^{188}\text{Hg}$  and  $^{190}\text{Hg}$  than in  $^{186}\text{Hg}$ , as observed experimentally. It should be noted that, for the ground-state and ND bands, the deformation parameters from the SCCM calculations are in good agreement with

those estimated from the experimental results, assuming the pure rotational (see Table II) and the other models.

The calculations also predict a band crossing at  $J^\pi = 6^+$  in  $^{188}\text{Hg}$  in agreement with the observations, i.e. the members of ND-prolate band becomes yrast at  $J = 6, 8, 10$ . In Table II the experimental reduced transition probabilities are compared with the SCCM calculation for  $^{188}\text{Hg}$ . The predictions are in good agreement for the ground-state band but, contrary to the IBM-CM case, the  $B(E2)$  value of the  $6_1^+ \rightarrow 4_1^+$  linking transition is underestimated; in addition, the predicted transition strengths in the intruder band are rather constant and the values are much larger than what is observed experimentally. These features can be interpreted as an underestimation of the possible mixing between the two bands. In fact, by looking at the CWFs (Figure 9), we see that the mixing between the different bands is very small because the overlaps between the CWFs are negligible. This fact might be related to the imposition of axial symmetry in the calculations. An exploratory calculation with  $N_{h.o.} = 11$  including triaxial shapes for the nucleus  $^{188}\text{Hg}$  suggests a larger mixing between the oblate and ND prolate configurations along the  $\gamma$  degree of freedom. However, such a computationally costly calculation did not converge with the number of harmonic oscillator shells and the prolate band was found to be the ground state configuration, contrary to what is obtained experimentally.

The underlying shell structure of the three collective bands can be also analysed within the SCCM framework. The relevant spherical shells that are needed to describe such states can be qualitatively identified by Nilsson-like orbits. These orbits are computed self-consistently for each nucleus with HFB states obtained along the quadrupole degree of freedom. As an example, the evolution of the spherical orbits as a function of the deformation,  $\beta_2$ , is plotted for the  $^{188}\text{Hg}$  isotope in Figure 10. The Fermi energies for protons and neutrons are also shown. The relevant regions, where the CWF are peaked (i.e. the minima of the energy surfaces), are marked by a grey band in the figure. In the oblate minimum, we see that the orbits close to the Fermi energy are:  $3s_{1/2}$ ,  $0h_{11/2}$  and  $0h_{9/2}$  for protons and  $0h_{9/2}$ ,  $1f_{7/2}$ ,  $0i_{13/2}$ ,  $2p_{3/2}$  and  $1f_{5/2}$  for neutrons. For the ND configuration, the  $1d_{5/2}$  and the  $1f_{7/2}$  for protons and the  $0g_{9/2}$  for neutrons also play a role. Finally, for the SD band, the  $0i_{11/2}$  and negative parity orbits above  $N = 126$  are also entering below the neutron Fermi energy. This picture shows the complexity of the single-particle structure of these heavy nuclei that prevents the use of shell model calculations. We compute the actual occupation numbers of spherical orbits with each individual SCCM wave functions in the three isotopes studied here following the method developed in Ref. [52]. To simplify the discussion about the occupancies, let us define a proton core of  $Z = 82$  that encompasses the  $0s$ ,  $0p$ ,  $1s-0d$ ,  $1p-0f$ ,  $2s-1d-0g$  and  $0h_{11/2}$  spherical orbits, and a neutron core of  $N = 100$  that includes the previous orbits plus the  $0h_{9/2}$  and  $1f_{7/2}$

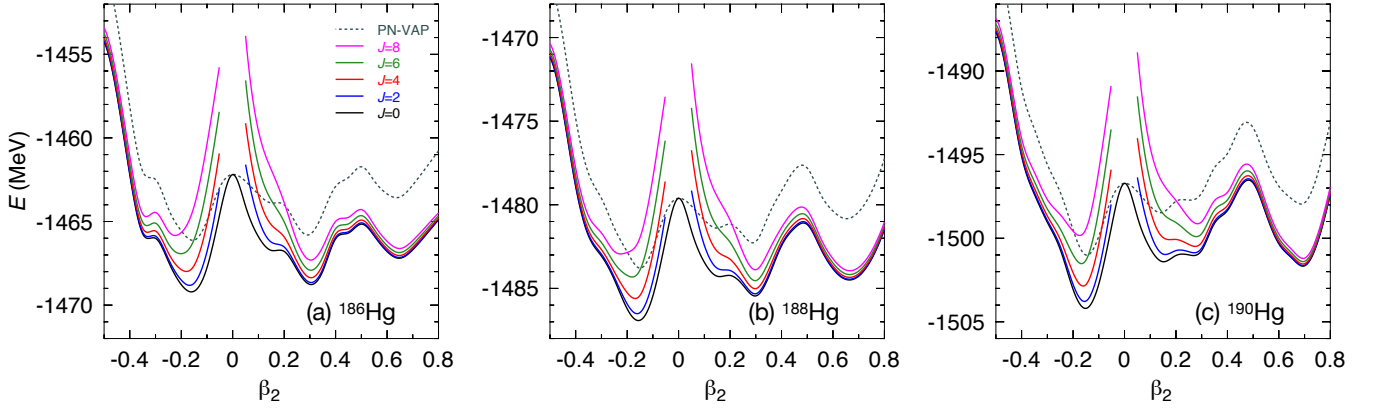


FIG. 7: (Color online) PN-VAP (dashed lines) and PNAMP (continuous lines) energy curves as a function of the axial quadrupole deformation  $\beta_2$  for the (a)  $^{186}\text{Hg}$ , (b)  $^{188}\text{Hg}$  and (c)  $^{190}\text{Hg}$  isotopes.

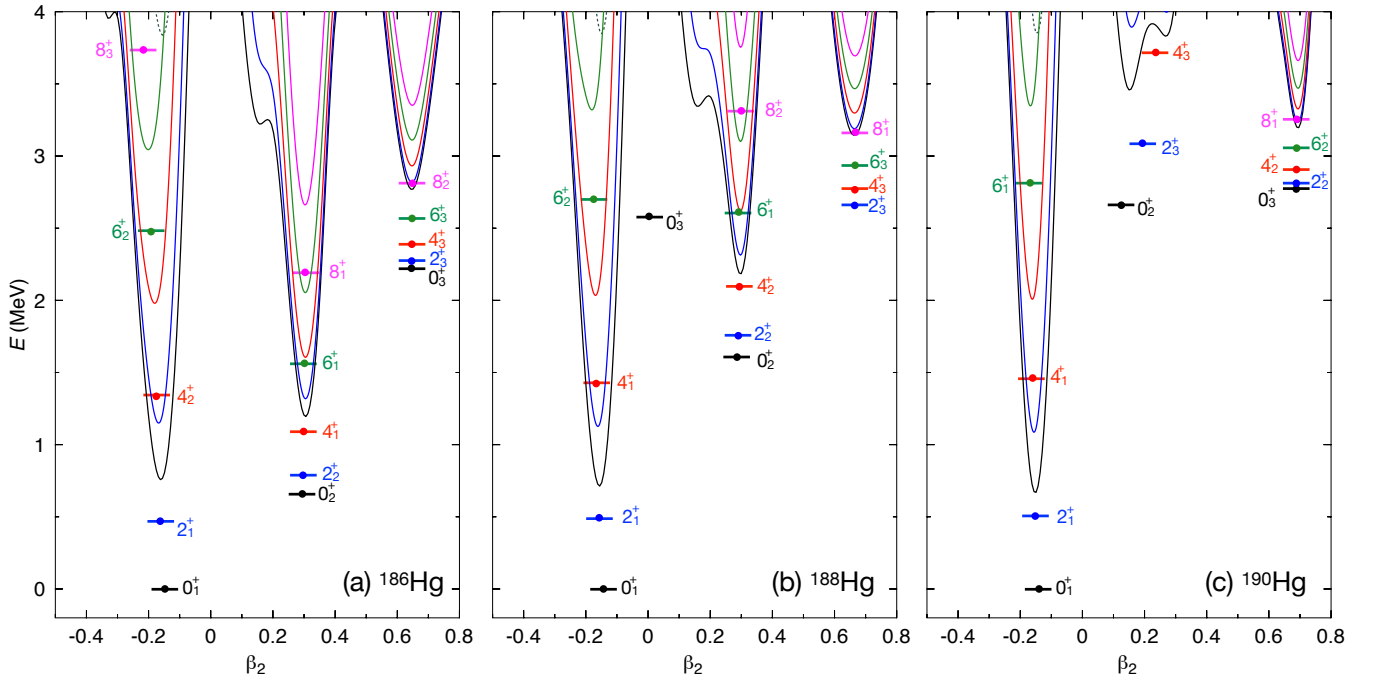


FIG. 8: (Color online) Spectra obtained with axial SCCM calculations with the Gogny D1S interaction for the (a)  $^{186}\text{Hg}$ , (b)  $^{188}\text{Hg}$  and (c)  $^{190}\text{Hg}$  isotopes. The energies are plotted at the mean value of the intrinsic quadrupole deformation of the corresponding collective wave functions. PNAMP energy curves as a function of  $\beta_2$  are also plotted to guide the eye.

neutron levels. Using such cores, the  $^{188}\text{Hg}$  isotope in a normal filling approximation should correspond to 2h-0p (protons) and 0h-8p (neutrons), respectively. However, the results obtained for the oblate, ND and SD bands are 4.0h-2.0p, 8.1h-6.1p and 9.0h-7.0p for protons, and 5.4h-13.4p, 7.7h-15.7p and 8.3h-16.3p for neutrons, respectively. Similar configurations are also obtained for the other two isotopes calculated here. These results show again the complexity of the single-particle structure driven by the deformation of the system.

## V. CONCLUSIONS

The nuclear structure of the neutron-deficient mercury was investigated via lifetime measurements at the Laboratori Nazionali di Legnaro. In order to control a possible contamination of the  $^{188}\text{Hg}$  data by other reaction channels, two different fusion-evaporation reactions were used for this study and, thanks to the powerful capabilities of both GALILEO and Neutron-Wall arrays, a clear identification of the channel of interest was possible.

Using the RDDS technique, the lifetimes of the states up to spin  $16\hbar$  were measured. The determined lifetimes of the  $2_1^+$  and  $4_1^+$  states are in agreement with

values reported in literature. Thanks to the new results for both low- and high-lying states, the deformation of the ground-state band and of the intruder structure was estimated from the experimental data, assuming two-band mixing and two different rotational models. These models provide a similar interpretation of the structures: the ground-state band has a quadrupole deformation of

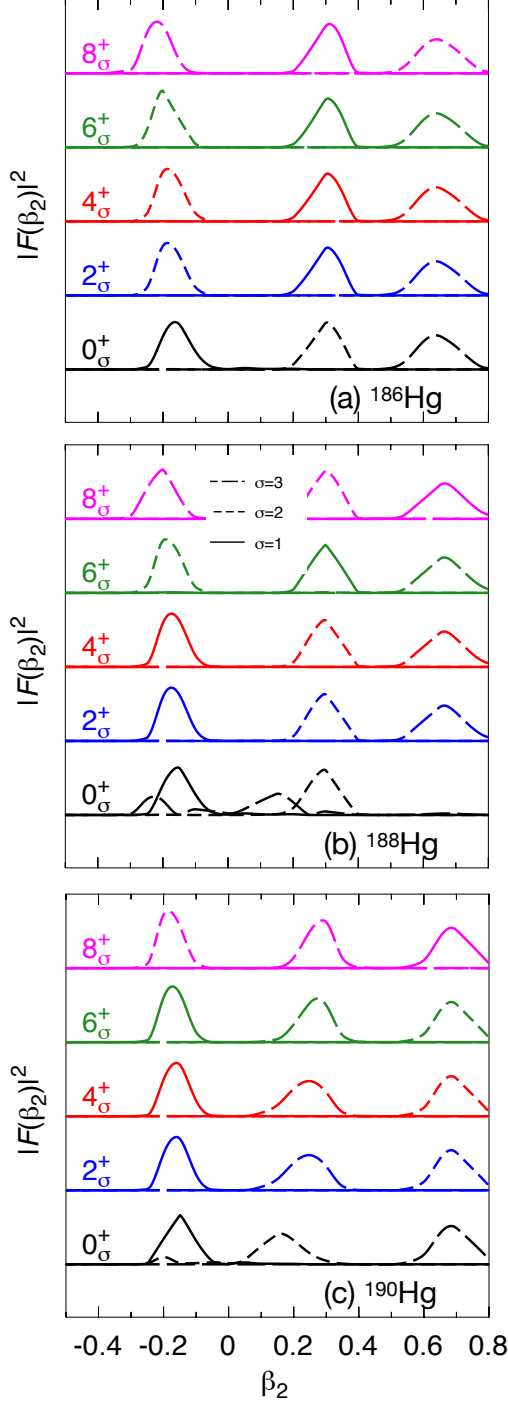


FIG. 9: (Color online) Collective wave functions (CWF) obtained with axial SCCM calculations with the Gogny D1S interaction for (a)  $^{186}\text{Hg}$ , (b)  $^{188}\text{Hg}$  and (c)  $^{190}\text{Hg}$  isotopes.

$\beta_2 \approx 0.13$ , while the intruder one has  $\beta_2 \approx 0.22$ . Moreover, the lifetimes of the  $14_1^+$  and  $16_1^+$  excited states highlighted the presence of an almost-spherical structure above the  $12_1^+$  isomer.

In the view of the new results, state-of-the-art SCCM calculations were performed for the even-mass  $^{186-190}\text{Hg}$  and predicted the presence of three structures in each of these nuclei, having oblate, normal- and super-deformed prolate deformation. The underlying shell structure of the three collective bands was analyzed within the SCCM framework, identifying the relevant spherical shells, necessary to describe such structures. For  $^{188}\text{Hg}$  the comparison between the theoretical predictions and the experimental results confirmed the proposed interpretation of both the intruder and ground-state bands. Further experimental investigations of the  $^{190}\text{Hg}$  are required to

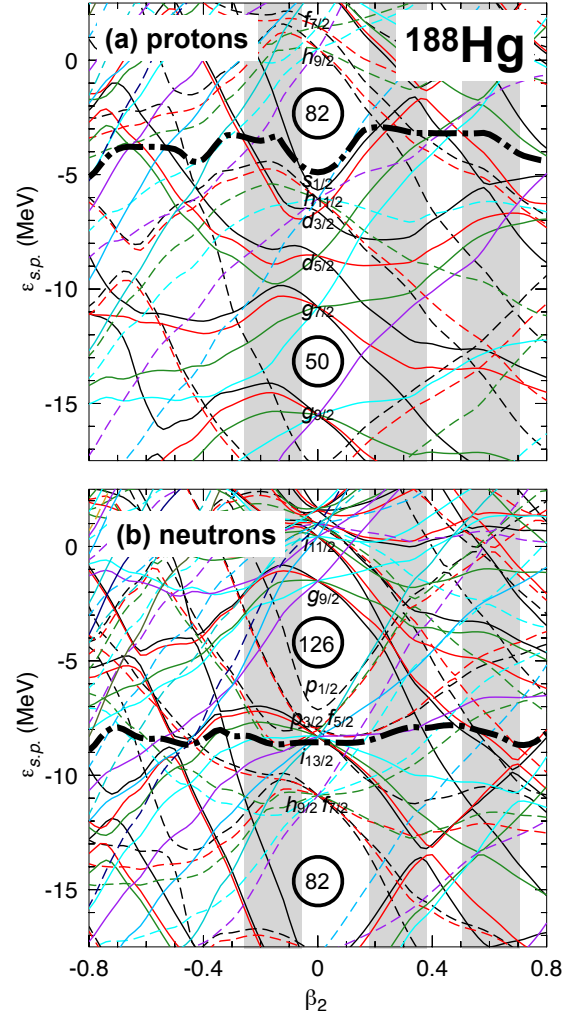


FIG. 10: (Color online) Single-particle energies for (a) protons and (b) neutrons as a function of the deformation  $\beta_2$  calculated for  $^{188}\text{Hg}$  with the Gogny D1S interaction. Dashed (continuous) lines represent negative (positive) parity states and the thick dashed-dotted lines show the Fermi energy. The shaded areas correspond to the position of the three minima in the energy surface shown in Figure 7.

resolve the ambiguity between the SCCM predictions and the previous calculations.

### Acknowledgements

The authors would like to thank the GALILEO collaboration. Special thanks go to the INFN-LNL technical staff for their help and the good quality beam and to Massimo Loriggiola for the extended work on the Gd plunger

targets. We acknowledge the numerical calculations of S. Hilaire. This paper owes much to the collaboration with P.E. Garrett. This work was partially supported by the Espace de Structure Nucléaire Théorique (CEA/DSM-DAM). The work was also supported (P.R.J. and P.K.) by the German BMBF under contract no. 05P18RDFN9, (G.J.) by the National Science Centre Poland (NCN) under the grant no. 2017/25/B/ST2/01569.

- 
- [1] T. Kühn, P. Dabkiewicz, C. Duke, H. Fischer, H.J. Kluge, H. Kremmling, E.W. Otten, *Phys. Rev. Lett.* **39**, 180 (1977)
  - [2] B. Marsh, T. Day Goodacre, S. Sels, Y. Tsunoda, B. Andel, A.N. Andreyev, N.A. Althubiti, D. Atanasov, A.E. Barzakh, J. Billowes et al., *Nature* **14**, 1163 (2018)
  - [3] A. Ansari, *Physics Review C* **33**, 321 (1986)
  - [4] P.R. John, V. Modamio, J.J. Valiente-Dobón, D. Mengoni, S. Lunardi, T.R. Rodríguez, D. Bazzacco, A. Gadea, C. Wheldon, T. Alexander et al., *Phys. Rev. C* **90**, 021301 (2014)
  - [5] P.R. John, J.J. Valiente-Dobón, D. Mengoni, V. Modamio, S. Lunardi, D. Bazzacco, A. Gadea, C. Wheldon, T.R. Rodríguez, T. Alexander et al., *Phys. Rev. C* **95**, 064321 (2017)
  - [6] A.N. Andreyev, M. Huyse, P. Van Duppen, L. Weissman, D. Ackermann, J. Gerl, F.P. Hessberger, S. Hofmann, A. Kleinbhl, G. Mnzenberg et al., *Nature* **405**, 430 (2000)
  - [7] P. Rahkila, D.G. Jenkins, J. Pakarinen, C. Gray-Jones, P.T. Greenlees, U. Jakobsson, P. Jones, R. Julin, S. Juutinen, S. Ketelhut et al., *Physics Review C* **82**, 011303 (2010)
  - [8] J. Bonn, G. Huber, H. Kluge, L. Kluger, E. Otten, *Physics Letter B* **38**(5), 308 (1972)
  - [9] I. Angeli, K. Marinova, *Atomic and Nuclear Data Table* **99**, 69 (2013)
  - [10] A. Sonzogni et al., *National Nuclear Data Center*
  - [11] J.D. Cole, J.H. Hamilton, A.V. Ramayya, W.G. Nettles, H. Kawakami, E.H. Spejewski, M.A. Ijaz, K.S. Toth, E.L. Robinson, K.S.R. Sastry et al., *Phys. Rev. Lett.* **37**, 1185 (1976)
  - [12] J.H. Hamilton, A.V. Ramayya, E.L. Bosworth, W. Lourens, J.D. Cole, B. Van Nooijen, G. Garcia-Bermudez, B. Martin, B.N.S. Rao, H. Kawakami et al., *Phys. Rev. Lett.* **35**, 562 (1975)
  - [13] J. Wauters, N. Bijnens, H. Folger, M. Huyse, H.Y. Hwang, R. Kirchner, J. von Schwarzenberg, P. Van Duppen, *Physics Review C* **50**, 2768 (1994)
  - [14] P. Joshi, E. Zganjar, D. Rupnik, S. Robinson, P. Mantica, H. Carter, J. Kormicki, R. Gill, W. Walters, C. Bingham et al., *International Journal of Modern Physics E* **3**(2), 757 (1994)
  - [15] G.D. Dracoulis, *Phys. Rev. C* **49**, 3324 (1994)
  - [16] L.P. Gaffney, M. Hackstein, R.D. Page, T. Grahm, M. Scheck, P.A. Butler, P.F. Bertone, N. Bree, R.J. Carroll, M.P. Carpenter et al., *Physical Review C* **89**, 024307 (2014)
  - [17] R.D. Page, A.N. Andreyev, D.R. Wiseman, P.A. Butler, T. Grahm, P.T. Greenlees, R.D. Herzberg, M. Huyse, G.D. Jones, P.M. Jones et al., *Physics Review C* **84**, 034308 (2011)
  - [18] E. Rapisarda, A.N. Andreyev, S. Antalic, A. Barzakh, T.E. Cocolios, I.G. Darby, R.D. Groote, H.D. Witte, J. Diriken, J. Elseviers et al., **44**(7), 074001 (2017)
  - [19] J.D. Cole, A.V. Ramayya, J.H. Hamilton, H. Kawakami, B. van Nooijen, W.G. Nettles, L.L. Riedinger, F.E. Turner, C.R. Bingham, H.K. Carter et al., *Phys. Rev. C* **16**, 2010 (1977)
  - [20] M. Scheck, P.A. Butler, L.P. Gaffney, N. Bree, R.J. Carroll, D. Cox, T. Grahm, P.T. Greenlees, K. Hauschild, A. Herzan et al., *Physics Review C* **83**, 037303 (2011)
  - [21] C. Müller-Gatermann, A. Dewald, C. Fransen et al., *Physics Review C* **99**, 054325 (2019)
  - [22] T. Grahm, A. Petts, M. Scheck, P.A. Butler, A. Dewald, M.B. Hornillos, P.T. Greenlees, A. Görgen, K. Helariutta, J. Jolie et al., *Physical Review C* **80**, 014324 (2009)
  - [23] M. Scheck, T. Grahm, A. Petts, P.A. Butler, A. Dewald, L.P. Gaffney, M.B. Hornillos, A. Görgen, P.T. Greenlees, K. Helariutta et al., *Physical Review C* **81**, 014310 (2010)
  - [24] N. Rud, D. Ward, H.R. Andrews, R.L. Graham, J.S. Geiger, *Physical Review Letter* **31**, 1421 (1973)
  - [25] D. Proetel, R. Diamond, F. Stephens, *Physical Review B* **48**, 102 (1974)
  - [26] W. Ma, A. Ramayya, J. Hamilton, S. Robinson, J. Cole, E. Zganjar, E. Spejewski, R. Bengtsson, W. Nazarewicz, J.Y. Zhang, *Physics Letters B* **167**(3), 277 (1986)
  - [27] B. Olaizola, A.B. Garnsworthy, F.A. Ali, C. Andreoiu, G.C. Ball, N. Bernier, H. Bidaman, V. Bildstein, M. Bowry, R. Caballero-Folch et al., *Physics Review C* **100**, 024301 (2019)
  - [28] A. Esmaylzadeh, L.M. Gerhard, V. Karayonchev, J.M. Régis, J. Jolie, M. Bast, A. Blazhev, T. Braunroth, M. Dannhoff, F. Dunkel et al., *Physical Review C* **98**(1), 014313 (2018)
  - [29] N. Bree, K. Wrzosek-Lipska, A. Petts, A. Andreyev, B. Bastin, M. Bender, A. Blazhev, B. Bruyneel, P.A. Butler, J. Butterworth et al., *Physical Review Letter* **112**, 162701 (2014)
  - [30] Wrzosek-Lipska, K., Rezynekina, K., Bree, N., Zielińska, M., Gaffney, L.P., Petts, A., Andreyev, A., Bastin, B., Bender, M., Blazhev, A. et al., *European Physics Journal A* **55**(8), 130 (2019)
  - [31] C. Praharaaj, S. Khadkikar, *J. Phys. G: Nucl. Phys.* **6**, 241 (1980)
  - [32] T. Nikšić, D. Vretenar, P. Ring, G. Lalazissis, *Physical Review C* **65**, 054320 (2002)
  - [33] C. Signorini, G. Bezzon, F. Cervellera, P. Spolaore,

- R. Ricci, Nuclear Instruments and Methods in Physics Research A **220**(1), 30 (1984)
- [34] A. Dainelli, G. Bassato, A. Battistella, M. Bellato, A. Beltramin, L. Bertazzo, G. Bezzon, G. Bisoffi, L. Boscagli, S. Canella et al., Nuclear Instruments and Methods in Physics Research A **382**, 100 (1996)
- [35] J. Valiente-Dobón, D. Mengoni, F. Recchia et al., INFN-LNL Report 2014 **241**, 95 (2015)
- [36] Ö. Skeppstedt, H. Roth, L. Lindström, R. Wadsworth, I. Hibbert, N. Kelsall, D. Jenkins, H. Grawe, M. Górska, M. Moszyński et al., Nuclear Instrumentation and Method in Physics Research A **421**, 531 (1999)
- [37] I. Zanon, M. Siciliano, P. John, A. Goasduff et al., INFN-LNL Report 2017 **251**, 62 (2018)
- [38] I. Zanon, M. Siciliano, P. John, A. Goasduff, Nuovo Cimento C **42**, 109 (2019)
- [39] A. Dewald, O. Möller, P. Petkov, Progress in Particle and Nuclear Physics **67**(3), 786 (2012)
- [40] C. Müller-Gatermann, F. von Spee, A. Goasduff, D. Baz-zacco, M. Beckers, T. Braunroth, A. Boso, P. Cocconi, G. de Angelis, A. Dewald et al., Nuclear Instruments and Methods A **920**, 95 (2019)
- [41] B. Saha, *Napatau or tk-lifetime-analysis* (2003)
- [42] G. Lane, G. Dracoulis, A. Byrne, S. Anderssen, P. Davidson, B. Fabricius, T. Kibdi, A. Stuchbery, A. Baxter, Nuclear Physics A **589**(1), 129 (1995)
- [43] J.E. García-Ramos, K. Heyde, Physics Review C **89**, 014306 (2014)
- [44] F. Kondev, S. Juutinen, D. Hartley, Nuclear Data Sheets **150**, 1 (2018)
- [45] E. Clément, A. Görden, W. Korten, E. Bouchez, A. Chatillon, J.P. Delaroche, M. Girod, H. Goutte, A. Hürstel, Y.L. Coz et al., Phys. Rev. C **75**, 054313 (2007)
- [46] K. Nomura, R. Rodríguez-Guzmán, L.M. Robledo, Phys. Rev. C **87**, 064313 (2013)
- [47] J.M. Yao, M. Bender, P.H. Heenen, Phys. Rev. C **87**, 034322 (2013)
- [48] J. Egido, Physica Scripta **91**(7), 073003 (2016)
- [49] L. Robledo, T. Rodríguez, R. Rodríguez-Guzmán, Journal of Physics G: Nuclear and Particle Physics **46**(1), 013001 (2018)
- [50] M. Anguiano, J. Egido, L. Robledo, Nuclear Physics A **696**(3), 467 (2001)
- [51] T. Rodríguez, A. Arzhanov, G. Martínez-Pinedo, Phys. Rev. C **91**, 044315 (2015)
- [52] T. Rodríguez, A. Poves, F. Nowacki, Phys. Rev. C **93**, 054316 (2016)